Electromagnetic Imaging for a Conducting Cylinder Buried in a Slab Medium by the Genetic Algorithm

Chun Jen Lin, Chun-Yuan Chou, Chien-Ching Chiu

Electrical Engineering Department, Tamkang University, Tamsui, Taiwan, R.O.C.

Received 27 July 2003; accepted 11 February 2004

ABSTRACT: This article presents a computational approach to the imaging of a perfectly conducting cylinder buried in a slab. A conducting cylinder of unknown shape buried in a slab scatters the incident wave from outside. The scattered field is recorded outside the slab. Based on the boundary condition and the measured scattered field, a set of nonlinear integral equations is derived, and the imaging problem is reformulated into an optimization problem. The genetic algorithm is then employed to determine global extreme solution of the cost function. Numerical results demonstrated that, even when the initial guess is far removed from the exact one, good reconstruction can be obtained. In such a case, the gradient-based methods often are trapped in a local extreme. In addition, the effect of Gaussian noise on the reconstruction is investigated. © 2004 Wiley Periodicals, Inc. Int J Imaging Syst Technol, 14, 1–7, 2004; Published online in Wiley InterScience (www.interscience.wiley.com). DOI 10.1002/ima.20000

Key words: electromagnetic imaging; slab medium; conductor; steady-state genetic algorithm

I. INTRODUCTION

The imaging problem of conducting objects has been a subject of considerable importance in noninvasive measurement, medical imaging, and biological application. In the past 20 years, many rigorous methods have been developed to solve the exact equation; however, inverse problems of this type are difficult to solve because they are ill posed and nonlinear. As a result, many inverse problems are reformulated as optimization problems. General speaking, two kinds of approaches have been developed. The first is based on gradient searching schemes such as the Newton–Kantorovitch method (Roger, 1981; Tobocman, 1989; Chiu and Kiang, 1991), the Levenberg–Marguart algorithm (Colton and Monk, 1986; Kirsch et al., 1988; Hettlich, 1994), and the successive overrelaxation method (Kleiman and van den Berg, 1994). These methods are highly dependent on the initial guess and tend to get trapped in a local extreme. In contrast, the second approach is based on evolutionary searching schemes (Xiao and Yabe, 1998; Chiu and Chen, 2000). They tend to converge to the global extreme of the problem, no matter what the initial estimate is (Goldberg, 1989; Rahmat-Samii and Michielssen, 1999). Owing to the difficulties in computing the Green's function by a numerical method, the problem of inverse scattering in a slab has seldom been tackled. To our knowledge, there are still no numerical results by the genetic algorithm for perfectly conducting scatterers buried in a slab.

In this article, we investigate the electromagnetic imaging of a perfectly conducting cylinder buried in a wall, using the steady-state genetic algorithm to recover the shape of the scatterer. It has been found that the steady-state genetic algorithm (Vavak and Fogarty, 1996; Johnson and Rahmat-Samii, 1997) can reduce the calculation time of the image problem compared with the generational genetic algorithm. We present the theoretical formulation for electromagnetic imaging in Section II, and describe the general principles of the genetic algorithm and the way in which we applied them to the imaging problem. We give the numerical results for various objects of different shapes in Section III and present our conclusions in Section IV.

II. THEORETICAL FORMULATION

A. Imaging Problem. Let us consider a two-dimensional slab structure as shown in Figure 1, where (ϵ_i, σ_i) $i = 1, 2, 3$ denote the permittivities and conductivities in each region. Here the permeabilities of all three regions are assumed to be μ_o, and a conducting cylinder is buried in region 2. The metallic cylinder with cross section described by the equation $\rho = F(\theta)$ is illuminated by an incident plane wave whose electric field vector is parallel to the Z-axis (i.e., TM polarization). We assume that the time dependence of the field is harmonic with the factor $\exp(j\omega t)$. Let E_{inc} denote the incident field ftom region 1 with incident angle θ_1 as follows:

$$E_{inc} = E_1^+ e^{+jk_1\cos\theta_1 y} e^{-jk_1\sin\theta_1 x}\hat{z}. \tag{1}$$

Owing to the interfaces, the incident plane wave generates three waves that would exist in the absence of the conducting object. Thus, the unperturbed field is given by

$$E = \begin{cases} E_1 = E_1^+ e^{+jk_1\cos\theta_1 y} e^{-jk_1\sin\theta_1 x}\hat{z} \\ \quad + E_1^- e^{-jk_1\cos\theta_1 y} e^{-jk_1\sin\theta_1 x}\hat{z}, & y \geq a \\ E_2 = E_2^+ e^{+jk_2\cos\theta_2 y} e^{-jk_2\sin\theta_2 x}\hat{z} \\ \quad + E_2^- e^{-jk_2\cos\theta_2 y} e^{-jk_21\sin\theta_2 x}\hat{z}, & a \geq y \geq -a \\ E_3 = E_3^+ e^{+jk_3\cos\theta_3 y} e^{-jk_3\sin\theta_3 x}\hat{z}, & y \leq -a \end{cases} \tag{2}$$

where E_1^+ is set to be 1 and

Correspondence to: Chien-Ching Chiu; e-mail: chiu@ee.tku.edu.tw

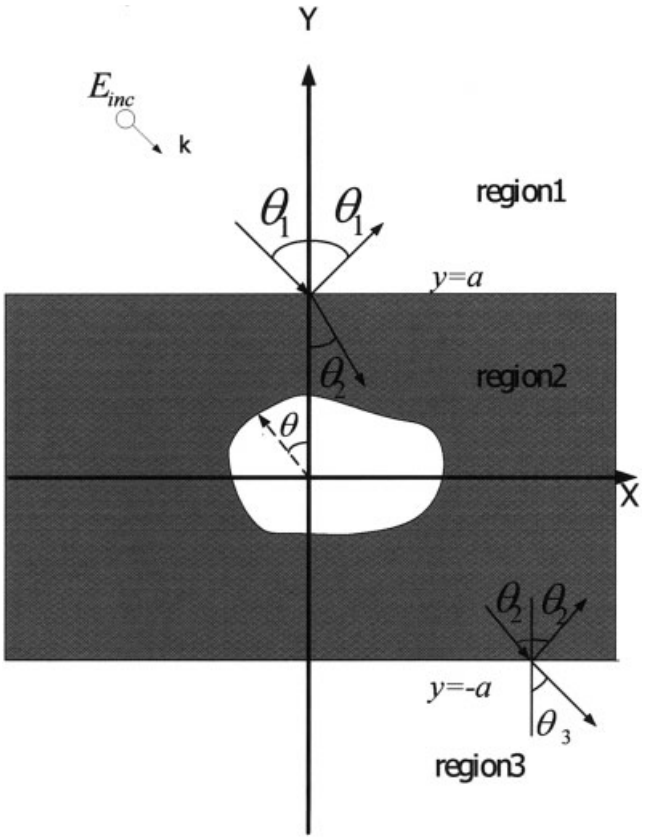

Figure 1. Geometry of the problem in (x, y) plane.

$$E_1^- = \frac{\begin{array}{r} e^{+j2k_1\cos\theta_1 a}[(Z_1+Z_2)(Z_3-Z_2)e^{-j2k_2\cos\theta_2 a} \\ -(Z_1-Z_2)(Z_3+Z_2)e^{+j2k_2\cos\theta_2 a} \end{array}}{\begin{array}{r} (Z_1+Z_2)(Z_3+Z_2)e^{+j2k_2\cos\theta_2 a} \\ -(Z_1-Z_2)(Z_3-Z_2)e^{-j2k_2\cos\theta_2 a} \end{array}}$$

$$E_2^+ = \frac{1}{2}\, e^{jk_2(\sin\theta_2 x - \cos\theta_2 a)}\left[\frac{Z_1+Z_2}{Z_1}\, e^{-jk_1(\sin\theta_1 x - \cos\theta_1 a)} + \frac{Z_1-Z_2}{Z_1}\, E_1^- e^{-jk_1(\sin\theta_1 x + \cos\theta_1 a)}\right]$$

$$E_2^- = \frac{1}{2}\, e^{jk_2(\sin\theta_2 x + \cos\theta_2 a)}\left[\frac{Z_1-Z_2}{Z_1}\, e^{-jk_1(\sin\theta_1 x - \cos\theta_1 a)} + \frac{Z_1+Z_2}{Z_1}\, E_1^- e^{-jk_1(\sin\theta_1 x + \cos\theta_1 a)}\right]$$

$$E_3^+ = \frac{2Z_3}{Z_2+Z_3}\, E_2^+ e^{-jk_2(\sin\theta_2 x + \cos\theta_2 a)}\, e^{jk_3(\sin\theta_3 x + \cos\theta_3 a)}$$

$$k_1\sin\theta_1 = k_2\sin\theta_2 = k_3\sin\theta_3$$

$$k_i^2 = \omega^2\varepsilon_i\mu_0 - j\omega\mu_0\sigma_i \qquad i = 1, 2, 3 \quad \mathrm{Im}(k_i) \le 0$$

$$Z_1 = \frac{\eta_1}{\cos\theta_1}, \quad Z_2 = \frac{\eta_2}{\cos\theta_2}, \quad Z_3 = \frac{\eta_3}{\cos\theta_3},$$

$$\eta_1 = \sqrt{\frac{\mu_0}{\varepsilon_1}}, \quad \eta_2 = \sqrt{\frac{\mu_0}{\varepsilon_2}}, \quad \eta_3 = \sqrt{\frac{\mu_0}{\varepsilon_3}}.$$

At an arbitrary point (x, y) [or (r, θ) in polar coordinates] in regions 1and 3 the scattered field, $\tilde{E}_s = \tilde{E} - \tilde{E}_i$, can be expressed as

$$E_s(\vec{r}) = -\int_0^{2\pi} G(\vec{r}, F(\theta'), \theta')J(\theta')\, d\theta', \tag{3}$$

where $J(\theta) = -j\omega\mu_0\sqrt{F^2(\theta) + F'^2(\theta)}J_s(\theta)$, $F(\theta)$ is the shape function, and $F'(\theta)$ is the differentiation of $F(\theta)$.

$$G(x, y; x', y') = \begin{cases} G_1(x, y; x', y'), & y > a \\ G_2(x, y; x', y'), & a > y > -a \\ G_3(x, y; x', y'), & y < -a \end{cases} \tag{4}$$

$$G_1 = \frac{1}{2\pi}\int_{-\infty}^{\infty} je^{-j\gamma_1(y-a)} \times \frac{(\gamma_2+\gamma_3)e^{j\gamma_2(y'+a)} + (\gamma_2-\gamma_3)e^{-j\gamma_2(y'+a)}}{(\gamma_1+\gamma_2)(\gamma_2+\gamma_3)e^{j\gamma_2(2a)} + (\gamma_1-\gamma_2)(\gamma_2-\gamma_3)e^{-j\gamma_2(2a)}} \times e^{-j\alpha(x-x')}\, d\alpha$$

$$G_2 = \frac{1}{2\pi}\int_{-\infty}^{\infty} \frac{j}{2\gamma_2} \times \left\{\left[\frac{\begin{array}{c}(\gamma_1+\gamma_2)(\gamma_2+\gamma_3)e^{-j\gamma_2[|y-y'|-2a]} \\ +(\gamma_2-\gamma_1)(\gamma_2-\gamma_3)e^{j\gamma_2[|y-y'|-2a]}\end{array}}{\begin{array}{c}(\gamma_1+\gamma_2)(\gamma_2+\gamma_3)e^{j\gamma_2(2a)} \\ +(\gamma_1-\gamma_2)(\gamma_2-\gamma_3)e^{-j\gamma_2(2a)}\end{array}}\right] + \left[\frac{\begin{array}{c}(\gamma_2-\gamma_1)(\gamma_2+\gamma_3)e^{j\gamma_2[y+y']} \\ +(\gamma_2-\gamma_3)(\gamma_1+\gamma_2)e^{-j\gamma_2[y+y']}\end{array}}{\begin{array}{c}(\gamma_1+\gamma_2)(\gamma_2+\gamma_3)e^{j\gamma_2(2a)} \\ +(\gamma_1-\gamma_2)(\gamma_2-\gamma_3)e^{-j\gamma_2(2a)}\end{array}}\right]\right\} e^{-j\alpha(x-x')}\, d\alpha$$

$$G_3 = \frac{1}{2\pi}\int_{-\infty}^{\infty} je^{j\gamma_3(y+a)} \times \left(\frac{(\gamma_1+\gamma_2)e^{-j\gamma_2(y'-a)} + (\gamma_2-\gamma_1)e^{j\gamma_2(y'-a)}}{(\gamma_1+\gamma_2)(\gamma_2+\gamma_3)e^{j\gamma_2(2a)} + (\gamma_1-\gamma_2)(\gamma_2-\gamma_3)e^{-j\gamma_2(2a)}}\right) \times e^{-j\alpha(x-x')}\, d\alpha,$$

with $\gamma_i^2 = k_i^2 - \alpha^2$, $i = 1, 2, 3$ and $\mathrm{Im}(\gamma_i) \le 0$.

Note that G_1, G_2, and G_3 denote the Green's function, which can be obtained by tedious mathematic manipulation for the line source in region 2. Note that we might face some difficulties in calculating the Green's function. The function, given by (4), is in the form of an improper integral that must be evaluated numerically. However, the integral converges very slowly when (x, y) and (x', y') approach the interface. Fortunately, we find that the integral in the Green's function may be rewritten as a closed-form term plus a rapidly converging integral (see Appendix). Thus, the whole integral in the Green's function can be calculated efficiently. $J_s(\theta)$ is the induced surface current density, which is proportional to the normal derivative of the electric field on the conductor surface. The boundary condition on the surface of the scatterer states that the total tangen-

tial electrical field must be zero and yield an integral equation for $J(\theta)$:

$$E_2(\vec{r}) = -\int_0^{2\pi} G_2(\vec{r}, F(\theta'), \theta')J(\theta')\, d\theta'. \quad (5)$$

For the direct scattering problem, the scattered field E_s is calculated by assuming that the shapes are known. This can be achieved by first solving J in (5) and then calculating E_s using (3). For the inverse problem, assume that the approximate center of the scatterer, which can be any point inside the scatterer, is known. Then the shape function $F(\theta)$ can be expanded as

$$F(\theta) = \sum_{n=0}^{N/2} B_n \cos(n\theta) + \sum_{n=1}^{N/2} C_n \sin(n\theta), \quad (6)$$

where B_n and C_n are real coefficients to be determined, and $N + 1$ is the number of unknowns for the shape function. Note that the discretization number of $J(\theta)$ for the inverse problem must be different from that for the direct problem. In our simulation, the discretization number for the direct problem is twice that for the inverse problem. It is crucial that the synthetic data generated through a direct solver are not like those obtained by the inverse solver. In the inversion procedure, the steady-state genetic algorithm is used to minimize the following cost function:

$$CF = \left\{ \frac{1}{M_t} \sum_{m=1}^{M_t} |E_s^{\exp}(\vec{r}_m) - E_s^{cal}(\vec{r}_m)|^2 / |E_s^{\exp}(\vec{r}_m)|^2 \right\}^{1/2}, \quad (7)$$

where M_t is the total number of measurement points. $E_s^{\exp}(\vec{r})$ and $E_s^{cal}(\vec{r})$ are the measured and calculated scattered fields, respectively.

B. Steady-State Genetic Algorithm. To the best of our knowledge, most (if not all) genetic algorithms (GA) use the uniform pdf to generate the random numbers needed during the course of offspring generation. We propose an improved, efficient SSGA version, called NU-SSGA, for which the bit string representation is kept and nonuniform beta distributions are introduced to help control the generation of offspring. Thus, in NU-SSGA, control over the granularity of representation is still possible, while the crossover and mutation operators are modified by incorporating the beta distribution such that the convergence speeds are improved for high-precision numerical optimization problems.

In general, a typical GA optimizer must be able to perform seven basic tasks (Johnson and Rahmat-Samii, 1997; Weile and Michielssen, 1997):

1. Encode the solution parameters as genes,
2. Create a string of the genes to form a chromosome,
3. Initialize a starting population,
4. Evaluate and assign fitness values to individuals in the population,
5. Perform reproduction through some selection scheme,
6. Perform recombination of genes to produce offspring, and
7. Perform mutation of genes to produce offspring.

In an NU-SSGA optimizer, task 2 is omitted, i.e., the strings of the parameters are not accumulated to form a chromosome as a typical GA optimizer does. For each individual, different parameters remain separated. In this case, the crossover operator for task 6 needs to be modified. A single-point crossover operator is used. Note that the new offspring is created by swapping the genetic materials of the corresponding parameters instead of the chromosomes, as is done in a typical GA (Weile and Michielssen, 1997).

Task 6 may be regarded as a modified N-point crossover version of the typical GA with one crossover point per parameter, where N is the number of parameters. The key distinction between an NU-SSGA and a typical GA is in the location of random crossover points. In a typical GA, the crossover points are randomly determined through a uniform probability density function (Weile and Michielssen, 1997), whereas, for an NU-SSGA, the crossover points are randomly and nonuninformly determined through other pdf's. The beta distributions are used in this article, of which the pdf's with different parameter pair are detailed in the reference (Rohatgi and Saleh, 2001). By changing the parameter pair adaptively, we can move the crossover points between the most significant bit (MSB) regions and the least significant bit (LSB) regions for different individuals. For those individuals for which the crossover points are around the MSB regions, NU-SSGA is in the phase of searching through the solution space with the parameters as largely spaced as possible, by which the diversity of the genetic distribution is maintained. On the other hand, when the crossover points are around the LSB regions, NU-SSGA is in the phase of speeding convergence, which is analogous to the mechanism of a local search algorithm. Similarly, the same distribution must be applied to the mutation operator for task 7 in accordance with the crossover operator. Finally, it should be noted that uniform pdf is still used for all the other tasks, such as the choice of parents for crossover and creation of initial population.

In our problem, both parameters B_n and C_n are encoded using Gray code. We employ NU-SSGA for the imaging problem investigated. We obtained new offspring by using a rank selection scheme. As soon as the cost function (CF) changes by $<1\%$ in two successive generations, the algorithm is terminated, and the final solution is then obtained.

It should be noted that the calculation of the Green's function is quite computationally expensive. NU-SSGA has not only a faster convergence characteristic (Johnson and Rahmat-Samii, 1997; Weile and Michielssen, 1997), but also a lower rate of crossover. As a result, it is a suitable scheme to save calculation time for the inverse problem as compared to the generational GA

III. NUMERICAL RESULTS

We illustrate the performance of the proposed inversion algorithm and its sensitivity to random noise in the scattered field. Consider a lossless three-layer structure ($\sigma_1 = \sigma_2 = \sigma_3$) and a perfectly conducting cylinder buried in region 2. The permittivity in each region is characterized by $\varepsilon_1 = \varepsilon_0$, $\varepsilon_2 = 2.55\varepsilon_0$, and $\varepsilon_3 = \varepsilon_0$, respectively, as shown in Figure 1. The frequency of the incident wave is chosen to be 1 GHz, with the incident angles equal to 45° and 315°, respectively. The width of the second layer is 0.3 m. Sixteen measurement points are equally separated on a circle of 3-m radius about center at equal spacing in region 1 and region 3. Thus there are 32 measurements in total in each simulation. The number of unknowns is set to be 9 (i.e., $N + 1 = 9$). The population size is chosen as 120. The coding length of each unknown coefficient, B_n (or C_n),

is set to be 16 bits. The search range for the unknown coefficient of the shape function is chosen to be from 0 to 0.1. The crossover probability p_c and mutation probability p_m are set to be 0.05 and 0.025.

In the first example, the shape function is chosen to be $F(\theta) = (0.06 + 0.01\cos 2\theta - 0.02\sin 2\theta)$ m. The reconstructed shape function for the best population member is plotted in Figure 2(a) with the shape error shown in Figure 2(b). The reconstructed result is quite good. Here, the shape function discrepancy is defined as

$$DR = \left\{ \frac{1}{N'} \sum_{i=1}^{N'} [F^{cal}(\theta_i) - F(\theta_i)]^2 / F^2(\theta_i) \right\}^{1/2}, \qquad (9)$$

where N' is set to 1000.

To investigate the sensitivity of the imaging algorithm against random noise, two independent Gaussian noises with zero mean are added to the real and imaginary parts of the simulated scattered fields. Normalized standard deviations of 10^{-4}, 10^{-3}, 10^{-2}, and 10^{-1} are used in the simulations. The normalized standard deviation is defined as the standard deviation of the Gaussian noise divided by the rms value of the scattered fields. Thus, the signal-to-noise ratio (SNR) is inversely proportional to the normalized standard deviation. The shape error vs. normalized noise level for example 1 is plotted in Figure 2(c). It is found that the effect of noise is negligible for normalized standard deviations below 10^{-2}.

In the second example, the shape function is chosen to be $F(\theta) = (0.05 + 0.01\cos 3\theta - 0.01\sin 3\theta)$ m. The purpose of this example is to show that the proposed scheme is able to reconstruct a scatterer whose shape has three concavities. The reconstructed shape function for the best population member is plotted in Figure 3(a), with the shape error shown in Figure 3(b). The reconstructed shape error is $<5\%$.

In the third example, the shape function is chosen to be $F(\theta) = (0.05 + 0.01\cos 4\theta - 0.01\sin 4\theta)$ m. The purpose of this example is to show that our method can reconstruct the scatterer whose shape function has four concavities. The reconstructed shape function for the best population member is plotted in Figure 4(a) with the error shown in Figure 4(b). The reconstructed shape error is $<5\%$.

IV. CONCLUSIONS

We have reported a study of applying the genetic algorithm to reconstruct the shapes of an embedded conducting cylinder. Based on the boundary condition and measured scattered field, we have derived a set of nonlinear integral equations and reformulated the imaging problem into an optimization problem. The genetic algorithm is then employed to de-embed the microwave image of a metallic cylinder. In our experience, the main difficulties in applying the genetic algorithm to the problem are to choose the suitable parameters, such as the population size, coding length of the string (L), crossover probability (p_c), and mutation probability (p_m). Different parameter sets will affect the speed of convergence as well as the computation time. Moreover, compared with the Newton–Kantorovitch algorithm, the genetic algorithm needs more computation time. However, accuracy, stability, and generality are better than in the Newton–Kantorovitch algorithm. Numerical results show that good reconstruction can be achieved as long as the normalized noise level is $<10^{-2}$.

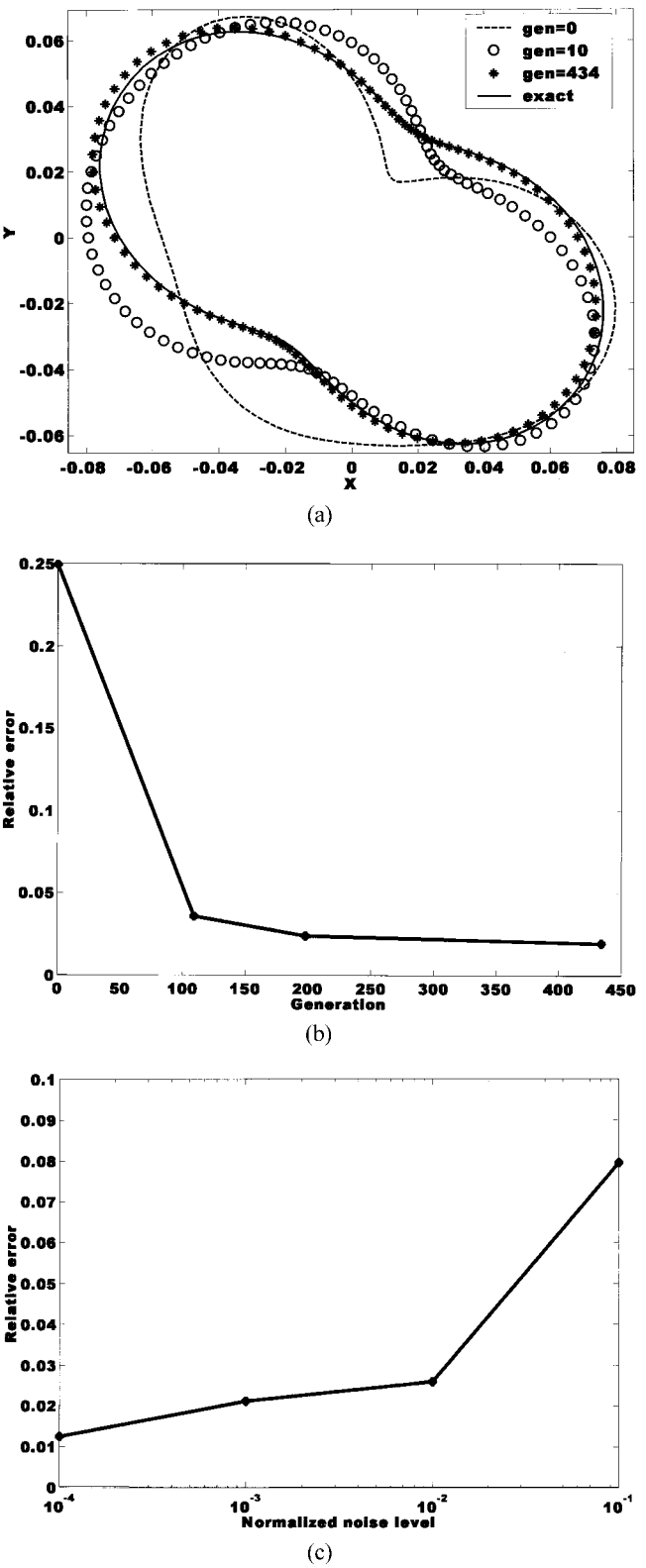

Figure 2. (a) Shape function for example 1. The solid curve represents the exact shape, while the dashed curves are calculated shape in iteration process. (b) Shape function error in each generation. (c) Shape function error as a function of noise levels for example 1.

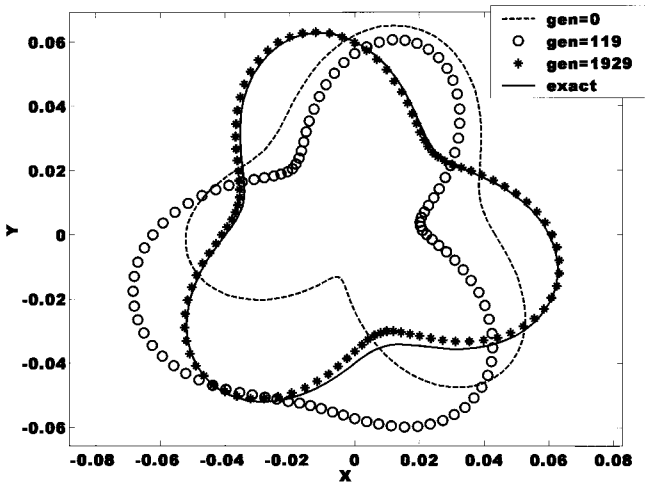

(a)

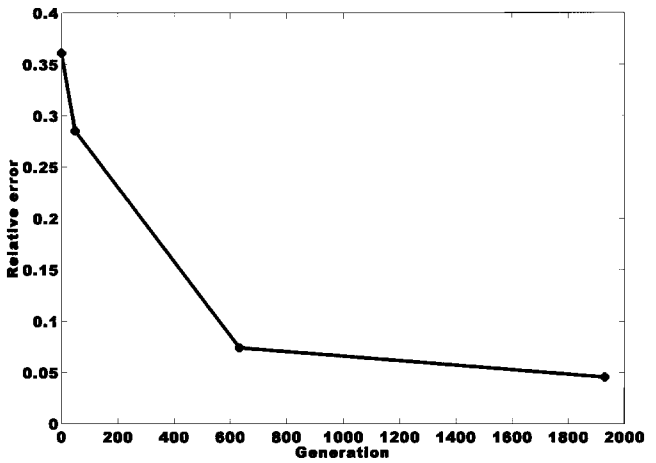

(b)

Figure 3. (a) Shape function for example 2. The solid curve represents the exact shape, while the dashed curves are calculated shape in iteration process. (b) Shape function error in each generation.

APPENDIX

To calculate the Green's function, we can use the following formula:

$$\int_u^\infty x^{r-1}e^{-\beta x}\cos\,\delta x\,dx = \frac{1}{2}(\beta + j\alpha)^{-r}\Gamma[r, (\beta + j\delta)u] + \frac{1}{2}(\beta - j\alpha)^{-r}\Gamma[r, (\beta - j\delta)u] \quad \text{for Re } \beta > |\text{Im } \delta| \quad \text{(A1)}$$

where $\Gamma(\alpha, Z) = \int_z^\infty e^{-t}t^{\alpha-1}\,dt$.

Γ is the incomplete gamma function, which has the following properties:

$$\Gamma(-n, z) = \frac{(-1)^n}{n!}\left[\Gamma(0, Z) - e^{-z}\sum_{m=0}^{n-1}(-1)^m\frac{m!}{z^{m+1}}\right]$$

$$\Gamma(0, z) = -\gamma - \ln z - \sum_{n=1}^{\infty}(-1)^n\frac{z^n}{(n+1)!} \quad [|\arg(z)| < \pi] \quad \text{(A2)}$$

in which γ is Euler's constant, i.e., $\gamma = 0.5772156649$.

Let us consider the following integral

$$G_1 = \frac{1}{2\pi}\int_{-\infty}^{\infty} je^{-jr_1(y-a)} \times \left(\frac{(r_2 + r_3)e^{jr_2(y'+a)} + (r_2 - r_3)e^{-jr_2(y'+a)}}{(r_1 + r_2)(r_2 + r_3)e^{jr_2(2a)} + (r_1 - r_2)(r_2 - r_3)e^{-jr_2(2a)}}\right) \times e^{-j\alpha(x-x')}\,d\alpha$$

$$= \frac{1}{\pi}\int_0^{\infty} je^{-jr_1(y-a)} \times \left(\frac{(r_2 + r_3)e^{jr_2(y'+a)} + (r_2 - r_3)e^{-jr_2(y'+a)}}{(r_1 + r_2)(r_2 + r_3)e^{jr_2(2a)} + (r_1 - r_2)(r_2 - r_3)e^{-jr_2(2a)}}\right) \times \cos\,\alpha(x - x')\,d\alpha,$$

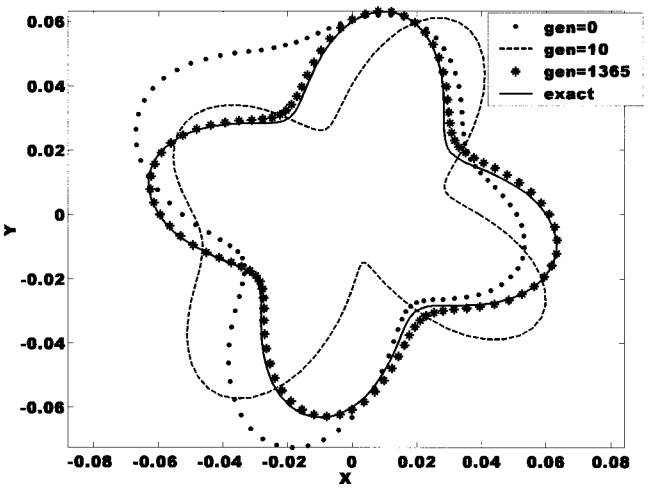

(a)

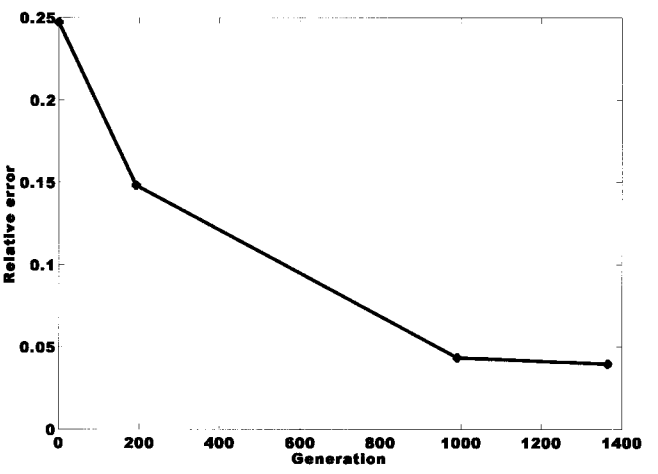

(b)

Figure 4. (a) Shape function for example 3. The solid curve represents the exact shape, while the dashed curves are calculated shape in iteration process. (b) Shape function error in each generation.

where $r_i^2 = k_i^2 - \alpha^2$, $i = 1, 2, 3$, $\mathrm{Im}(\gamma_i) \le 0$, $y \ge a$, $a \ge y' \ge -a$.

The integral G_1 may be rewritten as follows

$$G_1 = \frac{1}{\pi}\int_0^\infty je^{-jr_1(y-a)} \times \left(\frac{(r_2+r_3)e^{jr_2(y'+a)} + (r_2-r_3)e^{-jr_2(y'+a)}}{(r_1+r_2)(r_2+r_3)e^{jr_2(2a)} + (r_1-r_2)(r_2-r_3)e^{-jr_2(2a)}}\right) \times \cos\alpha(x-x')\,d\alpha$$

$$+\frac{1}{2\pi}\int_{\alpha_0}^\infty \left[\frac{e^{-\alpha(y-y')}}{\alpha} + \frac{(k_3^2-k_2^2)e^{-\alpha(y+y'+2a)}}{4\alpha^3}\right]\cos\alpha(x-x')\,d\alpha$$

$$-\frac{1}{2\pi}\int_{\alpha_0}^\infty \left[\frac{e^{-\alpha(y-y')}}{\alpha} + \frac{(k_3^2-k_2^2)e^{-\alpha(y+y'+2a)}}{4\alpha^3}\right]\cos\alpha(x-x')\,d\alpha.$$

In general, we choose $\alpha_0 \gg |k_i|$, $i = 1, 2, 3$.

By Eq. (A1), we get

$$-\frac{1}{2\pi}\int_{\alpha_0}^\infty \left[\frac{e^{-\alpha(y-y')}}{\alpha} + \frac{(k_3^2-k_2^2)e^{-\alpha(y+y'+2a)}}{4\alpha^3}\right]\cos\alpha(x-x')\,d\alpha = -\frac{1}{4\pi}\{\Gamma[0,[(y-y')+j(x-x')]\alpha_0] + \Gamma[0,[(y-y')-j(x-x')]\alpha_0]\} - \frac{(k_3^2-k_2^2)}{16\pi}\left\{\begin{array}{l}[(y+y'+2a)+j(x-x')]^2\Gamma[-2,[(y+y'+2a)+j(x-x')]\alpha_0] \\ +[(y+y'+2a)-j(x-x')]^2\Gamma[-2,[(y+y'+2a)-j(x-x')]\alpha_0]\end{array}\right\}.$$

Using the above relation, we obtain

$$G_1 = \frac{1}{\pi}\int_0^\infty je^{-jr_1(y-a)}\left(\frac{(r_2+r_3)e^{jr_2(y'+a)} + (r_2-r_3)e^{-jr_2(y'+a)}}{(r_1+r_2)(r_2+r_3)e^{jr_2(2a)} + (r_1-r_2)(r_2-r_3)e^{-jr_2(2a)}}\right)\cos\alpha(x-x')\,d\alpha$$

$$-\frac{1}{2\pi}\int_{\alpha_0}^\infty \left[\frac{e^{-\alpha(y-y')}}{\alpha} + \frac{(k_3^2-k_2^2)e^{-\alpha(y+y'+2a)}}{4\alpha^3}\right]\cos\alpha(x-x')\,d\alpha$$

$$-\frac{1}{4\pi}\{\Gamma[0,[(y-y')+j(x-x')]\alpha_0] + \Gamma[0,[(y-y')-j(x-x')]\alpha_0]\}$$

$$-\frac{(k_3^2-k_2^2)}{16\pi}\left\{\begin{array}{l}[(y+y'+2a)+j(x-x')]^2\Gamma[-2,[(y+y'+2a)+j(x-x')]\alpha_0] \\ +[(y+y'+2a)-j(x-x')]^2\Gamma[-2,[(y+y'+2a)-j(x-x')]\alpha_0]\end{array}\right\}. \quad \text{(A3)}$$

Now, the integral G_1 is written as a rapidly converging integral plus a dominate integral. We can use Eq. (A3) to evaluate G_1 by means of Simpson's rule easily.

Similarly,

$$G_2 = \frac{1}{\pi}\int_0^\infty \frac{j}{2r_2}\left\{\left[\frac{(r_1+r_2)(r_2+r_3)e^{-jr_2[|y-y'|-2a]} + (r_2-r_1)(r_2-r_3)e^{jr_2[|y-y'|-2a]}}{(r_1+r_2)(r_2+r_3)e^{jr_2(2a)} + (r_1-r_2)(r_2-r_3)e^{-jr_2(2a)}}\right]\right.$$

$$\left. + \left[\frac{(r_2-r_1)(r_2+r_3)e^{jr_2[y+y']} + (r_2-r_3)(r_1+r_2)e^{-jr_2[y+y']}}{(r_1+r_2)(r_2+r_3)e^{jr_2(2a)} + (r_1-r_2)(r_2-r_3)e^{-jr_2(2a)}}\right] - \frac{je^{-jr_2|y-y'|}}{2r_2}\right\}\cos\alpha(x-x')\,d\alpha$$

$$+\frac{j}{4}H_0^{(2)}(k_2\sqrt{(x-x')+(y-y')}) + \frac{1}{2\pi}\int_{\alpha_0}^\infty \left[\begin{array}{c}\dfrac{(k_3^2-k_2^2)(k_1^2-k_2^2)e^{-\alpha[4a-|y-y'|]}}{16\alpha^5} \\ +\dfrac{(k_1^2-k_2^2)}{4}\dfrac{e^{-\alpha(2a-y-y')}}{\alpha^3} + \dfrac{(k_3^2-k_2^2)}{4}\dfrac{e^{-\alpha(y'+y+2a)}}{\alpha^3}\end{array}\right]\cos\alpha(x-x')\,d\alpha$$

$$-\frac{(k_1^2-k_2^2)}{16\pi}\left\{\begin{array}{l}[(2a-y-y')+j(x-x')]^2\Gamma[-2,[(2a-y-y')+j(x-x')]\alpha_0] \\ +[(2a-y-y')-j(x-x')]^2\Gamma[-2,[(2a-y-y')-j(x-x')]\alpha_0]\end{array}\right\}$$

$$-\frac{(k_3^2-k_2^2)}{16\pi}\left\{\begin{array}{l}[(y+y'+2a)+j(x-x')]^2\Gamma[-2,[(y+y'+2a)+j(x-x')]\alpha_0] \\ +[(y+y'+2a)-j(x-x')]^2\Gamma[-2,[(y+y'+2a)-j(x-x')]\alpha_0]\end{array}\right\}$$

$$-\frac{(k_1^2-k_2^2)(k_3^2-k_2^2)}{64\pi}\left\{\begin{array}{l}[4a-|y-y'|+j(x-x')]^4\Gamma[-4,[4a-|y-y'|+j(x-x')]\alpha_0] \\ +[4a-|y-y'|-j(x-x')]^4\Gamma[-4,[4a-|y-y'|-j(x-x')]\alpha_0]\end{array}\right\}.$$

And

$$G_3 = \frac{1}{2\pi}\int_{-\infty}^{\infty} je^{jr_3(y+a)}\left(\frac{(r_1+r_2)e^{-jr_2(y-a)}+(r_2-r_1)e^{jr_2(y-a)}}{(r_1+r_2)(r_2+r_3)e^{jr_2(2a)}+(r_1-r_2)(r_2-r_3)e^{-jr_2(2a)}}\right)e^{-j\alpha(x-x')}\,d\alpha$$

$$= \frac{1}{\pi}\int_{0}^{\infty} je^{jr_3(y+a)}\left(\frac{(r_1+r_2)e^{-jr_2(y'-a)}+(r_2-r_1)e^{jr_2(y'-a)}}{(r_1+r_2)(r_2+r_3)e^{jr_2(2a)}+(r_1-r_2)(r_2-r_3)e^{-jr_2(2a)}}\right)e^{-j\alpha(x-x')}\,d\alpha$$

$$+\frac{1}{2\pi}\int_{\alpha_0}^{\infty}\left[\frac{e^{-\alpha(y'-y)}}{\alpha}+\frac{(k_1^2-k_2^2)e^{-\alpha(2a-y-y')}}{4\alpha^3}\right]\cos\,\alpha(x-x')\,d\alpha-\frac{1}{4\pi}\{\Gamma[0,[(y'-y)+j(x-x')]\alpha_0]+\Gamma[0,[(y'-y)-j(x-x')]\alpha_0]\}$$

$$-\frac{(k_1^2-k_2^2)}{16\pi}\left\{\begin{array}{l}[(2a-y-y')+j(x-x')]^2\Gamma[-2,[(2a-y-y')+j(x-x')]\alpha_0]\\+[(2a-y-y')-j(x-x')]^2\Gamma[-2,[(2a-y-y')-j(x-x')]\alpha_0]\end{array}\right\}$$

REFERENCES

C.C. Chiu and W.T. Chen, Electromagnetic imaging for an imperfectly conducting cylinder by the genetic algorithm. IEEE Trans Microwave Theory Technol 48 (2000), 901–1905.

C.C. Chiu and Y.W. Kiang, Electromagnetic imaging for an imperfectly conducting cylinders. IEEE Trans Microwave Theory Technol 39 (1991), 1632–1639.

D. Colton and P. Monk, A novel method for solving the inverse scattering problem for time-harmonic acoustic waves in the resonance region II. SIAM J Appl Math 46 (1986), 506–523.

D.E. Goldberg, Genetic Algorithms in Search, Optimization, and Machine Learning. Reading, MA: Addison-Wesley, 1989.

F. Hettlich, Two methods for solving an inverse conductive scattering problem. Inverse Problems 10 (1994), 375–385.

J.M. Johnson and Y. Rahmat-Samii, Genetic algorithms in engineering electromagnetics. IEEE Antennas Propagat Mag 39 (1997), 7–21.

R.E. Kleiman and P.M. van den Berg, Two-dimensional location and shape reconstruction. Radio Sci 29 (1994), 1157–1169.

A. Kirsch, R. Kress, P. Monk, and A. Zinn, Two methods for solving the inverse acoustic scattering problem. Inverse Problems 4 (1988), 749–770.

Y. Rahmat-Samii and E. Michielssen, Electromagnetic Optimization by Genetic Algorithms. New York: Wiley Interscience, 1999.

A. Roger, Newton–Kantorovitch algorithm applied to an electromagnetic inverse problem. IEEE Trans Antennas Propagat AP-29 (1981), 232–238.

V.K. Rohatgi and A.K.Md.E. Saleh, An Introduction to Probability and Statistics, 2nd ed. New York: John Wiley & Son, 2001.

W. Tobocman, Inverse acoustic wave scattering in two dimensions from impenetrable targets. Inverse Problems 5 (1989), 1131–1144.

F. Vavak and T.C. Fogarty, Comparison of steady state and generational genetic algorithms for use in nonstationary environments. Proc IEEE International Conference on Evolutionary Computation, (1996), pp. 192–195.

S. Weile and E. Michielssen, Genetic algorithm optimization applied to electromagnetics: A review. IEEE Trans Antennas Propagat 45 (1997), 343–353.

F. Xiao and H. Yabe, Microwave imaging of perfectly conducting cylinders from real data by micro genetic algorithm coupled with deterministic method. IEICE Trans Electron E81-C(12) (1998), 1784–1792.